Contrasting snow and ice albedos derived from MODIS, Landsat ETM+ and airborne data from Langjökull, Iceland

Pope, E.[1,2], I. C. Willis[1], A. Pope[1,3], E. S. Miles[1], N. S. Arnold[1], and W. G. Rees[1]

[1] Scott Polar Research Institute, University of Cambridge, Lensfield Road, Cambridge CB2 1ER, UK.

[2] National Oceanography Centre, University of Southampton Waterfront Campus, European Way, Southampton SO14 3ZH, UK.

[3] National Snow and Ice Data Center, University of Colorado, Boulder, 1540 30th St, CO 80303, United States.

Abstract: Surface albedo is a key parameter in the energy balance of glaciers and ice sheets because it controls the shortwave radiation budget, which is often the dominant term of a glacier's surface energy balance. Monitoring surface albedo is a key application of remote sensing and achieving consistency between instruments is crucial to accurate assessment of changing albedo. Here we take advantage of a high resolution (5 m) airborne multispectral dataset that was collected over Langjökull, Iceland in 2007, and compare it with near contemporaneous ETM+ and MODIS imagery. All three radiance datasets are converted to reflectance by applying commonly used atmospheric correction schemes: 6S and FLAASH. These are used to derive broadband albedos. We first assess the similarity of albedo values produced by different atmospheric correction schemes for the same instrument, then contrast results from different instruments. In this way we are able to evaluate the consistency of the available atmospheric correction algorithms and to consider the impacts of different spatial resolutions. We observe that FLAASH leads to the derivation of surface albedos greater than when 6S is used. Albedo is shown to be highly variable at small spatial scales. This leads to consistent differences associated with specific facies types between different resolution instruments, in part attributable to different surface bi-directional reflectance distribution functions. Uncertainties, however, still exist in this analysis as no correction for variable bi-directional reflectance distribution functions could be implemented for the ETM+ and airborne datasets.

Key words:- Albedo measurement, Landsat, MODIS, Snow, Ice, Glacier, Ice cap, spatial scales, FLAASH, 6S

Corresponding Author: Ed.Pope@noc.soton.ac.uk

1. Introduction

A key concern associated with rising high northern latitude temperatures is the melting of terrestrial ice bodies leading to the rise of global sea levels (Dowdeswell et al. 1997; Hagen et al. 2003; Meier et al. 2007; Radić and Hock 2011; Wolken et al. 2009). Arctic and sub-Arctic ice masses are particularly sensitive to climate change as temperatures there are rising at about twice the global average (Graversen et al. 2008). Predicting the response of terrestrial ice bodies to high northern latitude climate change requires accurate calculation of surface melt rates and thus precise assessment of the ice surface energy-balance (Aas et al. 2015). In many systems, energy balance studies have shown that net shortwave radiation is often the dominant contributor of available energy for melting glacier snow and ice (Arendt 1999). The amount of energy available to glacier surfaces from shortwave fluxes is controlled by the surface albedo, i.e. its reflectivity. Accurate measurement and parameterisation of surface albedo is therefore a key component in calibrating/validating energy balance models designed to estimate past, current and future glacier melt. This is particularly important in Arctic and sub-Arctic regions because a key reason why high northern latitude temperatures are rising so rapidly is due to albedo feedbacks (Serreze et al. 2007).

Glacier surface reflectance can be measured using either *in situ* ground based methods or remote sensing techniques (Cutler and Munro 1996; Reijmer et al. 1999). Satellite and airborne remote sensing allows both large spatial coverage and regular temporal sampling, and limits the cost and risk associated with repeat field measurements (Aniya et al. 1996; Box et al. 2012; Boyd 2009; Paul et al. 2004). The various instruments on board different remote sensing platforms use a range of spectral bands which require geometric and atmospheric correction to convert radiance to

51 reflectance, and Narrow-To-Broadband (NTB) transformation to produce average surface
52 reflectance. The suitability of individual sensors for energy balance studies depends, therefore, on
53 the spectral and spatial resolution of individual sensors, the reliability of geometric/atmospheric
54 correction techniques, and the precision of the NTB transformation (Chander et al. 2009; Greuell and
55 Oerlemans 2004; Rees 2006; Vermote et al. 2002).

56 The albedo of glacier snow and ice is highly spatially and temporally variable. It depends on a range
57 of factors including solar incidence angle, cloud cover, surface topography, snow grain size and
58 geometry, impurities in the snow and ice, and water content (Arnold et al. 2006; Dumont et al. 2012;
59 Warren and Wiscombe 1980; Wiscombe and Warren 1980). Albedo varies over spatial scales on the
60 order of meters (Arnold and Rees 2003) and it evolves temporally as snow metamorphoses and
61 melts or as new snow falls (Brock et al. 2000). Surface albedo and its association with different snow
62 and ice facies has been monitored throughout the year in a range of climatic settings (Box et al.
63 2012; Klok and Oerlemans 2002; Tedesco et al. 2011). Fresh snow can have an albedo of over 0.9
64 whereas ice can range between ~0.4 and ~0.1 depending on the debris content (Cuffey and
65 Paterson 2010).

66 Many studies have attempted to compare satellite derived albedos with ground measurements and
67 to improve the algorithms used to derive surface albedo from satellite data (Greuell et al. 2002; Hall
68 et al. 1989; Hendriks and Pellikka 2004; Knap and Reijmer 1998; Liang et al. 2005; Reijmer et al.
69 1999; Stroeve et al. 2005). Such studies use mainly ground point measurements and are therefore
70 limited by their lack of spatial and temporal resolution. Regarding spatial resolution, point
71 measurements have sometimes been used to validate measurements for pixels with areas up to 1
72 km^2. Despite their frequent use, point measurement validations rely on relatively homogeneous
73 surface reflectance characteristics in the surrounding areas. This is frequently not the case,
74 especially for valley glaciers and the outlet glaciers from ice caps and ice sheets.

Greuell et al. (2002) sought to improve on ground point measurements using helicopter-based albedo readings. However, the spatial coverage of this study was still rather limited, equating to a few thousand data points. By contrast, in the present study, we use 1.32 x 10^7 measurements derived from a high resolution Airborne Thematic Mapper (ATM) dataset to validate both Landsat 7 Enhanced Thematic Mapper Plus (ETM+) and MODerate Resolution Imaging Spectroradiometer (MODIS) albedo data. The primary aims of our study are to assess the spatial pattern of surface albedo across an ice mass and to evaluate the consistency of different scientific products derived from various remote sensing instruments. The study is applied to Langjökull, a typical Icelandic ice mass, which exhibits a large range of albedos both spatially across the ice cap and temporally through the year.

2. Study site and data

2.1 Study site

Langjökull (64.7°N, 20.4°W) is Iceland's second largest ice cap, with an area of ~925 km^2 (Fig. 1). The ice cap elevation ranges from 450 to 1450 m above sea level with an average height of 900 m (Pope et al. 2013). Langjökull is surrounded by basalt lava fields, sandur plains and proglacial lakes and while two major rivers drain some meltwater from the ice cap, a significant proportion drains directly into the substrate to feed groundwater aquifers (Guðmundsson 2009). The ice cap's surface energy balance is dominated by the short-wave radiation flux with short-term peaks in sensible and latent heat fluxes contributing significantly to ablation only occasionally (Björnsson and Pálsson 2008). These peaks result from spells of high temperatures, moist air and katabatic winds driven by albedo contrasts between the glacier surface and surrounding regions. Understanding the albedo variability of ice masses such as Langjökull and parameterising this for use in energy balance models is therefore crucial for calculating mass balance changes in response to regional climate changes (Flowers et al. 2007; Guðmundsson 2009). Obtaining accurate data on surface albedo at a high spatial and temporal resolution is therefore an important stage in this process. The size of the ice

cap means that the findings should be useful for other large ice masses in the sub-Arctic and Arctic, including the Greenland Ice Sheet.

2.2 Airborne Thematic Mapper (ATM)

Our ATM dataset is derived from a Daedalus 1268 passive multispectral scanner mounted on a Dornier 228 aircraft flown by the UK National Environment Research Council (NERC) Airborne Research and Survey Facility (ARSF). It was collected during an aerial campaign over Langjökull on 2 August 2007 between 14:21 and 17:50 UTC. The whole of Langjökull was imaged in 24 separate, overlapping strips covering 11 wavelength bands in the visible, near, short and thermal infrared regions of the electromagnetic spectrum (Table 1).

Table 1: ATM band information.

Band	**Wavelengths (nm)**	**Spectral Response**
1	420-450	Ultraviolet/blue
2	450-520	Blue
3	520-600	Green
4	600-620	Yellow/orange
5	630-690	Red
6	690-750	Near-infrared
7	760-900	Mid-infrared
8	910-1050	Mid-infrared
9	1550-1750	Shortwave-infrared
10	2080-2350	Mid-infrared
11	8500-13000	Thermal-infrared

2.2.1 ATM swath preparation

The ARSF provided the data in individual swaths as at-sensor calibrated radiance. However, before atmospheric corrections could be applied limb brightening effects needed to be removed. Limb brightening is the result of larger viewing angles (i.e. the further away from nadir the greater the brightening), as a consequence of the increased path length and therefore atmosphere that a signal must pass through. As such, a swath correction must be applied to ensure that the data are radiometrically homogeneous (Palubinskas et al. 2003a, b; Zhao et al. 2005). Ideally these

corrections for viewing angle dependent would have been made using a physical model based on *in situ* measurements; however, such data are unavailable. Instead, an empirical multiplicative correction based on a 5th order polynomial was fitted to each swath, having taken the average brightness for each cross-swath pixel for each entire flight line (Hill et al. 2010):

$$L(a) \approx c_1 a^5 + c_2 a^4 + c_3 a^3 + c_4 a^2 + c_5 a + c_6 \quad (1)$$

where a is the angle from nadir measured across the swath, L(a) is fitted mean radiance for a given view angle (-45° to 45° for the ATM). Assuming that the view angle effects are minimal when the view angle is zero, a multiplicative correction function (K_{mult}) is identified such that:-

$$K_{mult}(a) = L(a)/L(a = 0) \quad (2)$$

where L(0) is the fitted mean radiance at swath centre, which is assumed to be nadir. This correction function is then applied to all pixels such that:-

$$L'(a, y) = L(a, y)/Kmult(a) \quad (3)$$

where L'(a,y) is the corrected radiance for a given angle and position along the flight line, respectively (Kennedy et al. 1997; Palubinskas et al. 2003b).

The corrected swaths were then orthorectified and gridded to 5 m (according to aircraft altitude and scan rate) using AZGCORR and the ASTER GDEM as a topographic input. Each swath was interpolated to an output image on a regular grid in a recognised map projection coordinate space aligned at a fixed spheroid height.

Having produced the Level 3A product, the swaths were manually geolocated using a Landsat 7 ETM+ image from 20 August 2000 (path 219, row 15) to allow precise comparison of the ATM and the satellite images. This image was chosen due to the high geolocational accuracy of Landsat 7 data (Lee et al. 2004; Tucker et al. 2004) and the particular scene's low cloud cover. Low-variability features, located principally in proglacial areas, were selected as control points.

2.3 Landsat Enhanced Thematic Mapper Plus (ETM+)

The ETM+ dataset containing eight different spectral bands has the higher spatial resolution of the two satellite datasets used (Table 2). The image selected was collected on 15 August 2007 (path 220, row 15) as it was closest in time to the acquisition dates of both the ATM and the MODIS data (2 August 2007 and 5 August 2007, respectively).

Table 2. ETM+ band information.

Band Number	Wavelength Interval (nm)	Spectral Response	Spatial Resolution (m)
1	452-514	Blue-Green	30
2	519-601	Green	30
3	631-692	Red	30
4	772-898	Near Infrared	30
5	1547-1748	Shortwave Infrared	30
6	10310-12360	Thermal Infrared	30
7	2065-2346	Mid-infrared	30
8	515-896	Panchromatic	15

2.4 Generating narrowband albedo for ATM and ETM+

To generate narrowband albedos from the ATM swaths and the ETM+ image, two different atmospheric correction models were used. First, they were corrected using the Fast Line-of-sight Atmospheric Analysis of Spectral Hypercubes (FLAASH) atmospheric model implemented in ENVI (Matthew et al. 2000; Perkins et al. 2012). FLAASH derives the atmospheric properties for each pixel in an image using look-up tables generated through MODTRAN-4. The ATM and ETM+ datasets corrected using the FLAASH atmospheric model are henceforth referred to as ATMFlaash and ETMFlassh, respectively.

Second, they were corrected using the 6S model (Kotchenova and Vermote 2007; Vermote et al. 2006). Unlike FLAASH, 6S is not generalised but exploits user-supplied measurements of atmospheric aerosol, ozone, and water content, and the corrections should therefore reflect more precisely the location and time of the ATM and ETM+ datasets than those made using FLAASH (Mahiny and Turner

2007). However, the 6S code was developed for application at a single-point (or pixel), due to its many required inputs. Therefore, the LandCor Matlab routines (Zelazowski et al. 2011) were used to distribute the 6S atmospheric transfer code across the individual ATM swaths and the entire ETM+ scene. LandCor determines representative atmospheric constituents and scene-sensor-sun geometries across the swaths/image, allowing a multidimensional lookup table of corrections to be developed, which is then applied to the source data. For this study, atmospheric constituents were determined from MODIS and Total Ozone Mapping Spectrometer (TOMS) records corresponding to the image acquisition time. The ATM and ETM+ datasets corrected using 6S are referred to, respectively, as ATM6S and ETM6S.

2.5 Narrow to broadband conversion

Having carried out the radiance to reflectance transformations for each band, the narrowband spectral reflectances were converted to average surface reflectance, i.e. broadband albedo, using an empirical relationship established initially using Landsat 5 TM data (Knap et al. 1999). It is acceptable for use on the ATM and ETM+ data because ATM bands 3 and 7, and ETM+ bands 2 and 4 are comparable with Landsat 5 TM bands 2 and 4 used by Knap et al. (1999). The relationship has also been validated for Vatnajökull (Reijmer et al. 1999), which is likely to have similar characteristics to Langjökull. Thus, the broadband albedos were calculated from:-

$$\alpha_{broadband} = 0.726r_{Green} - 0.322r_{Green}^2 - 0.015r_{NIR} + 0.581r_{NIR}^2 \quad (4)$$

2.6 MODIS

At 500 m posting, the lowest resolution dataset used was the MODIS Bi-directional Reflectance Distribution Function (BRDF)/Albedo product (MCD43), assigned the date 5 August 2007. The MCD43 product contains two sets of measurements; ‘white sky’ and ‘black sky’. The white-sky albedo calculation assumes homogeneous, full hemisphere irradiance while the black-sky albedo derivation assumes that all irradiance is from the point of solar illumination; both methods correct the observed radiance by using the view angle and a Bidirectional Reflectance Distribution Function

185 (BRDF) (Schaaf et al. 2002; Schaepman-Strub et al. 2006). This study uses the black-sky product as it
186 is comparable to the ATM and ETM+ generated data.

187 The MCD43 product is generated every eight days using 16 days of acquired MOD09 and MYD09
188 images and is made up of seven spectral bands (Table 3). It is derived from basic algorithms applied
189 to cloud-free atmospherically corrected surface reflectance values which have been corrected using
190 6S (Liang et al. 2005; Lucht et al. 2000; Privette et al. 1997; Roujean et al. 1992; Schaaf et al. 2002;
191 Strahler et al. 1999). The four MOD09 and MYD09 images used to generate the MCD43 product used
192 in this study were collected between 5 August 2007 and 20 August 2007 making the product
193 temporally comparable with the ATM dataset (2 August 2007) but a little earlier than the ETM+
194 dataset (15 August 2007). Analysis of the BRDF/Albedo quality for the selected image using the
195 MCD43A2 product showed that 61% of pixels were 'good quality' and had undergone full inversions
196 and 39% were of 'best quality' and had undergone full inversions. The quality of the image is
197 therefore good enough for comparison with the other datasets.

198 *Table 3. Selected MODIS MOD09 and MYD09 band information.*

Band number	Wavelength interval (nm)	Resolution (m)
1	620-670	250
2	841-876	250
3	459-479	500
4	545-565	500
5	1230-1250	500
6	1628-1652	500
7	2105-2155	500

199

200 The MCD43 BRDF/Albedo product algorithm is widely accepted for use in surface reflectance studies
201 due to regular comparisons with *in situ* point measurements (Salomon et al. 2006; Stroeve et al.
202 2005).

203 **2.6.1 Narrow to broadband albedo conversion for MODIS**

As MODIS bands do not have the same spectral response as those of either the ATM or the ETM+, the NTB algorithm is distinct and of critical importance. Here, we use an NTB conversion coefficient specifically designed for deriving broadband albedos for high albedo snow (Stroeve et al. 2005). Only the spectral wavelengths from 300 to 3000 nm (shortwave albedo) are considered due to their dominance of the solar spectrum. The conversion formula for the shortwave broadband albedo (α_{short}) is given by:-

$$\alpha_{short} = -0.0093 + 0.1574r_1 + 0.2789r_2 + 0.3829r_3 + 0.1131r_5 + 0.0694r_7 \quad (5)$$

where *r* is the MODIS narrowband reflectance from the specified MODIS spectral channel (Stroeve et al. 2005).

2.7 Cloud removal

Although the automated processing of MODIS imagery removes any cloud cover, this is not the case for the ATM or ETM+. As the ATM acquisition occurred on a cloudless day, cloud covered areas only have to be removed from the ETM+ image. Cloud was removed from this image using an NDSI threshold value of 0.75, a value used in other studies (Shimamura et al. 2006). The removal of cloud covered areas from both the ETM+ and MODIS imagery means that subsequent albedo analysis is limited primarily to southern areas of the ice cap, specifically the outlet glaciers Svartárjökull, Flosaskarðsjökull, Lónjökull, Vestari-Hagafellsjökull, Eystri-Hagafellsjökull and Suðurjökull (Fig. 1).

3. Results

Results are divided into two parts. First, for both the ATM and ETM+ datasets, the effects of the different processing techniques (i.e. FLAASH and 6S) are analysed. Second, differences between the albedo estimates generated by the different instruments (ATM, ETM+ and MODIS) are compared. The spatial extent of all the datasets is the same, as each dataset has been masked to the full extent of available albedo values across all datasets.

3.1. ATM dataset comparison

The ATMFlaash and ATM6S datasets are similar, with albedo varying strongly with elevation (Fig. 2a and 2b). Low but slightly varying albedo surfaces, interpreted as ice with varying debris concentrations, are found at lower elevations with higher albedo surfaces, interpreted as snow, present at high elevations. The transition zone between these two areas occurs at elevations between 900 and 1100 m and is interpreted to be a mixture of snow, firn and ice occurring in close association. The ATMFlaash dataset has a mean albedo of 0.364 with a standard deviation of 0.131. The ATM6S mean albedo is lower (0.326) and is statistically different from the ATMFlaash dataset (Tables 4 and 5).

Table 4. Descriptive statistics for Langjökull albedo calculated using various sensors and atmospheric correction algorithms.

	ATMFlaash	**ATM6S**	**ETMFlaash**	**ETM6S**	**MCD43 (MODIS)**
Minimum	0.026	0.036	0.010	0.310	0.068
Maximum	0.679	0.600	0.913	0.649	0.626
Mean	0.364	0.326	0.437	0.341	0.363
Standard Deviation	0.131	0.149	0.141	0.224	0.136

Table 5. Results of two tailed t-test for all dataset combinations. Each dataset is statistically different from all other datasets.

	t-statistic	**P-value**
ATMFlaash – ATM6S	-681.79	$p < 0.001$
ATMFlaash – ETMFlaash	-376.89	$p < 0.001$
ATMFlaash – ETM6S	94.22	$p < 0.001$
ATMFlaash – MCD43	-1.83	0.067
ATM6S – ETMFlaash	-575.54	$p < 0.001$
ATM6S – ETM6S	-61.65	$p < 0.001$
ATM6s – MCD43	-15.74	$p < 0.001$
ETMFlaash – ETM6S	-314.56	$p < 0.001$
ETMFlaash – MCD43	24.93	$p < 0.001$
ETM6S – MCD43	-10.22	$p < 0.001$

Similarities and differences between the ATMFlaash and ATM6S albedo datasets are indicated by Fig. 3a and Fig. 3b. The figures show that the two albedo processing methods produce broadly similar

albedo responses. Both generate bimodal albedo frequency distributions, one part representing snow, the other ice. The parts of the distributions representing ice are similar in terms of peak, spread and shape but the parts representing snow have subtle differences. The part of the distribution representing snow in the ATMFlaash dataset has a greater spread and correspondingly the pixel count for any value is lower. The modal snow albedo, where the highest pixel count occurs is also greater for the ATMFlaash dataset (~0.486) compared to that for the ATM6S dataset (~0.454).

The discrepancy between the two datasets is caused solely by differences in the atmospheric correction models. FLAASH has attributed a smaller proportion of at-sensor retrieved light to atmospheric scattering and absorption compared to 6S. Stated another way, 6S has removed a greater atmospheric contribution through the use of atmospheric column data appropriate to the day of measurement compared to the use of atmospheric data generalised for latitude and time of year within FLAASH. The result is that surface albedo values are generally higher for ATMFlaash than for ATM6S. The atmospheric correction carried out by FLAASH is also dependent, unlike 6S, on the contents and size of the image. 6S has a water and aerosol content specific to each pixel whereas FLAASH uses the ratio of specific bands to account for atmospheric contents. Changing the size or composition of the scene corrected by FLAASH will therefore have a large impact on derived albedo. The atmospheric model performance with regards to flight direction for individual swaths also differs. 6S appears able to correct for the non-Lambertian scattering over the ice cap surface, as a correction for flight direction was incorporated into the code when 6S was run. FLAASH was less able to correct for the non-Lambertian scattering as no flight direction correction was incorporated. The inability to correct for this effect results in striping which can be seen in Fig. 2a, but not in Fig. 2b.

3.2. ETM+ dataset comparison

The ETM+ dataset comparison shows similar characteristics to the comparison of the ATM datasets (Fig. 2). Both the ETMFlaash and ETM6S datasets show that elevation is the principle control on

surface albedo. The transition between snow and ice occurs between ~900 and 1100 m elevation. As with the ATM datasets, the mean albedo was greater and the values are more variable when corrected using FLAASH than when corrected with 6S (Table 4). The ETMFlaash mean albedo is 0.437. The ETM6S mean albedo is 0.341. Fig. 3c and Fig. 3d show these differences. As exhibited by the ATM datasets, the overall form of the ETM+ dataset albedo frequency distributions is similar. Both datasets have bimodal frequency distributions, however, the ETMFlaash dataset exhibits a number of unique features, when compared with all other datasets (Fig. 3). The parts of the frequency distributions representing ice and snow in the ETMFlaash dataset are much more spread than those in any of the other datasets. They are also centred on higher albedo values, respectively 0.294 and 0.683 compared to 0.232 and 0.489 for the ETM6S dataset. As with the differences between the two ATM datasets, the differences here are also probably caused solely by differences in the atmospheric correction models used. FLAASH has again attributed a smaller proportion of at-sensor retrieved light to atmospheric scattering and absorption compared to 6S. The result is the surface values are generally higher for the ETMFlaash dataset compared to the ETMFlaash dataset.

3.3. Inter-instrument comparison

Comparison of the five datasets shows distinct differences in derived albedos (Fig.2; Fig.3; Table 4; Table 5). The ATM and ETM+ datasets corrected using 6S have the lowest mean albedos, the MCD43 dataset has the next lowest mean albedo. The two datasets corrected using FLAASH have the highest mean values. The ATM6S, ETM6S and MCD43 albedo distributions also have relatively low and comparable standard deviations and overall ranges. The FLAASH corrected datasets have both the highest standard deviations of albedo values and the greatest albedo ranges as is indicated by the greater dispersion of the parts of the frequency distributions representing snow and ice; this is particularly true of the ETMFlaash dataset. However, the MCD43 dataset also shows some differences when compared with the ATM6S and ETM6S datasets. The parts of its distribution associated with snow and ice are centred at ~0.569 and ~0.295 respectively. The snow frequency

295 peak is slightly greater than the corresponding peak of the ATM6S and ETM6S datasets. The
296 frequency peak for ice is comparable to that in the ATM6S and ETM6S. The range of snow albedos
297 measured by the MCD43 dataset is small compared to the other datasets although the absolute
298 number of grids depicting snow is relatively high and so its mean albedo is slightly higher than that
299 for the ATM6S and ETM6S datasets.

300 The discrepancies between the two ETM+ datasets (Figs. 3c and d) are greater than those between
301 the two ATM datasets (Figs. 3a and b). This is most likely the result of the greater transmission
302 distance through the atmosphere for the satellite data compared to the airborne data. The greater
303 distance and therefore the greater atmospheric scattering and absorption associated with the
304 satellite data exaggerates differences between the atmospheric structures used by the two models.

305 Below, we focus further analysis on the three datasets deemed to be the most accurate: ATM6S,
306 ETM6S and MCD43. This decision was made on the basis that FLAASH was unable to remove the
307 striping in the airborne dataset (Fig. 2a) and produced very different albedo values compared to the
308 other datasets (Figs 2c and 3c). Furthermore, 6S is commonly used and frequently evaluated
309 (Mahiny and Turner 2007) and with no ground truth *in situ* data available in this study, the use of
310 one similar atmospheric correction model across all three datasets allows for a better comparison.

311 **3.3.1. Comparison of pixel values across Langjökull**

312 To assess the impact of image resolution on capturing albedo variability, datasets from the different
313 platforms were compared at the scale of individual pixels. This was done in two ways. First, each
314 lower resolution dataset was resampled using nearest neighbour interpolation to the resolution of
315 each higher resolution dataset. Second, each higher resolution dataset was resampled to that of
316 each lower resolution dataset by taking the arithmetic mean of all the pixels in the former that are
317 contained within each pixel of the latter. For each comparison, both the Root Mean Square Errors

318 and the Pearson correlation-coefficients are analysed. The two types of resampling produce virtually

319 identical results (Tables 6 and 7).

320

Table 6. Correlation between ATM6S, ETM6S and MCD43 datasets where the lower resolution data are resampled to the pixel sizes of the higher resolution data.

Dataset comparison	RMSE	Pearson correlation coefficient
ATM6S – ETM6S	0.087	0.767
ATM6S – MCD43	0.092	0.787
ETM6S – MCD43	0.076	0.814

Table 7. Correlation between ATM6S, ETM6S and MCD43 datasets where the higher resolution data are resampled to the pixel sizes of the lower resolution data.

Dataset comparison	RMSE	Pearson correlation coefficient
ATM6S – ETM6S	0.086	0.780
ATM6S – MCD43	0.095	0.792
ETM6S – MCD43	0.079	0.820

Both the RMSE and correlation statistics show that the best match between any two datasets is between the two satellite images: ETM6S and MCD43, where 277 pixels in the former are compared with each pixel in the latter. The ATM6S data are less well matched with both the ETM6S and the MCD43 data. As we might expect, the error is largest between the two datasets that have the greatest resolution difference, the ATM6S and the MCD43, where 10,000 pixels in the former make up each pixel in the latter, and the error is slightly lower between the ATM6S and the ETM6S datasets, where 36 pixel of the former are compared with each pixel of the latter. The correlation, measuring the overall strength of the relationship between the two variables, is slightly greater for the ATM6S – MCD43 comparison than for the ATM – ETM6S comparison, reflecting the lower scatter about a linear trend through the two variables of the former compared to the latter. Given the differences in resolution, processing techniques, and dates of acquisition, all these comparisons are very good. The RMSE results show that the 500 m MCD43 dataset captures the spatial heterogeneity of albedo in the 30 m ETM6S dataset better than the ETM6S image captures the heterogeneity seen in the 5 m ATM6S image.

The impacts of different spatial resolutions on derived albedos can be seen in Figs. 4 and 5. As instrument resolution decreases, the extent of local spatial variability seen in the higher resolution datasets is increasingly lost. Fig. 5 shows the standard deviation of albedo values of each of the higher resolution datasets within each of the pixels of the lower resolution datasets. It shows that

343 the variability of albedo within each low resolution pixel varies as a combined function of both
344 elevation and facies type. Albedo variability is highest in the transition area and to a slightly lesser
345 extent in the high albedo snow facies. The variability is lowest in the moderately dirty ice region and
346 areas of very dirty ice near the glacier margin.

347 To investigate the similarities and discrepancies in albedo measurements between the three
348 datasets further, difference maps were produced by subtracting the pixel values of the lower
349 resolution dataset from the values in the higher resolution dataset (Fig. 6). The maps show that
350 differences between the datasets are spatially correlated. A comparison of the ATM6S and ETM6S
351 datasets reveals four zones (Fig. 6a). At higher elevations corresponding to high albedo snow facies,
352 ATM6S albedos are less than ETM6S albedos. This is true also at mid elevations in the ablation area
353 corresponding to moderately dirty ice facies. Between these two areas is the transition zone facies
354 where the reverse is true; there, ATM6S albedos are greater than ETM6S albedos. Similarly, over
355 very dirty ice facies at low elevations around the glacier margin ATM6S albedos are larger than
356 ETM6S albedos. The mean difference over the ice cap between the two datasets is -0.013 whilst the
357 difference range is -0.504 – 0.570.

358 A comparison of the ATM6S and MCD43 datasets also reveals the four zones of snow, transition
359 zone, moderately dirty ice and very dirty ice from high elevations to the glacier margin where the
360 ATM6S minus MCD43 difference alternates between negative and positive (Fig. 6b). The mean
361 difference (-0.036) is greater than that for the ATM6S-ETM6S comparison (Fig. 6a) although the
362 range is slightly smaller (-0.475 – 0.444). The higher spatial resolution of Fig. 6a compared to Fig. 6b
363 is clearly shown, resulting in the former picking out greater spatial heterogeneity of differences
364 between the two datasets, than the latter. This is particularly visible in the high albedo snow facies
365 and dirty ice facies of Vestari-Hagafellsjökull and Eystri-Hagafellsjökull. Despite the different
366 resolutions at which the comparisons are made, most of the systematic discrepancies seen in Fig. 6a
367 are also present in Fig. 6b.

368 The four facies zones of snow, the transition, moderately dirty ice and very dirty ice discussed above
369 are not so clearly visible in the ETM6S minus MCD43 comparison (Fig. 6c). The overall mean
370 difference between the datasets is -0.022, whilst the difference range is (-0.606 – 0.386). The ETM6S
371 albedos are greater than those of the MCD43 dataset in the transition zone and the dirty ice facies
372 near the margins. The ETM6S albedos are lower than those of the MCD43 dataset in the high albedo
373 snow facies and the moderately dirty ice facies.

374 **4. Discussion**

375 The discussion is divided into three parts. First, we outline the possible reasons for the differences
376 between the ATM6S, ETM6S and MCD43 datasets. Second, we evaluate the MCD43 product against
377 the ATM6S and ETM6S datasets. Last, we assess the implications of the differences between the
378 datasets for energy balance modelling and melt estimates.

379 **4.1. Reasons for differences between the datasets**

380 *(i) Different processing techniques*

381 One reason for the differences between the three datasets is the different processing techniques
382 used to generate the narrowband albedos. Specifically, processing carried out to generate the
383 MCD43 dataset accounts for BRDF, which attempts to correct for the anisotropy of the surface
384 reflectance (Liang et al. 2005; Stroeve et al. 2005).The BRDF correction is determined by the
385 weighted sum of an isotropic parameter and two functions (kernels) of viewing and illumination
386 geometry (Roujean et al. 1992). Over glacier surfaces, the kernel weights that best fit the majority
387 situation are selected after image pixels have been interpreted as snow-covered or snow-free (Lucht
388 et al. 2000; Schaaf et al. 2002). In contrast, processing using only 6S as was the case for the ATM6S
389 and ETM6S datasets assumes the surface has a uniform BRDF (Kotchenova and Vermote 2007).

390 If difference in processing technique alone were the dominant factor explaining contrasts between
391 the datasets we would expect the ATM6S and ETM6S datasets to be similar to each other and both

very different to the MCD43 dataset. Fig. 6 shows that the ATM6S and ETM6S datasets are no more similar to one another than they are to the MCD43 dataset. We observe four zones where the measured albedos have similar differences between the datasets (snow, transition zone, moderately dirty ice and very dirty ice facies). Critically, the size of the differences between the ATM6S and ETM6S datasets is on average greater than that between the ETM6S and MCD43 datasets. The differences between the datasets also have the same sign, i.e. the high resolution datasets measure higher albedos in the dirty ice and transition zone facies, but measure lower albedos in the snow and moderately dirty ice facies. These comparisons show that the ATM6S and ETM6S processed datasets which assume a uniform BRDF, are not more similar to one another than they are to the MCD43 product assuming a non-uniform BRDF. Differences in accounting for surface anisotropy are therefore not the single dominant reason for variations between the datasets.

(ii) Different acquisition times

Assuming no new snowfall, the overall surface albedo of Langjökull would be expected to drop over the ablation season. Given the acquisition dates of the ATM (2 August), MODIS (5 – 20 August), and ETM+ (15 August) we would expect differences to be positive everywhere in Fig. 6a, positive everywhere in Fig. 6b and negative everywhere in Fig. 6c. The difference maps (Fig.6) and mean differences show this not to be the case. In every comparison, negative mean values are obtained by subtracting the low resolution dataset values from the high resolution dataset. Furthermore, for Fig. 6a we would also expect the overall mean difference to be the largest as a consequence of the temporal difference between the two datasets being the greatest. The mean difference between the datasets is in fact the smallest (-0.013). Instead, the mean difference is greatest between the ATM6S and MCD43 datasets (-0.036). Only the average difference between the ETM6S and MCD43 datasets (Fig. 6c) implies that temporal evolution has resulted in the overall difference between the datasets (-0.022). However, closer inspection of Fig. 6c implies additional controls. Whilst snowline migration could be seen to result in the large positive areas seen in Figs. 6a and 6b, a large proportion of the

same region has a positive difference between the two datasets in Fig. 6c. This would not be expected if snowline migration alone was the dominant cause of this area of difference and implies there are additional reasons for the large differences seen in this region in Figs 6a and 6b. These observations imply that temporal evolution and darkening of the surface albedo was not the dominant control causing the differences between the datasets.

(iii) Biases due to the different spatial resolutions of the three datasets

The fundamental contrast between the datasets is the spatial resolution of the instruments used to capture surface albedo. It is clear from Fig. 6 that there are large differences between the high resolution 5 m ATM6S dataset, the medium resolution 30 m ETM6S dataset and the lowest resolution 500 m MCD43 datasets. In both Fig. 6a and Fig. 6b there are very few pixels where the datasets agree closely on surface albedo. The differences between the 30 m ETM6S dataset and the 500 m MCD43 datasets are smaller but still apparent (Fig. 6c). If resolution alone were responsible for these differences we would expect that the closer the resolution between the two datasets, the lower the difference between them to be when the high resolution dataset is resampled to the pixel size of the lower resolution dataset. However, the RMSE data in Table 7, and the apparent zonation of differences on Fig. 6 show this not simply to be the case.

Coarsening the high resolution dataset by averaging the pixel values across the pixel size of the low resolution dataset does not result in the datasets becoming more comparable. Nevertheless, instrument resolution is probably the dominant cause of the over and underestimation of albedo associated with specific facies in the coarser instrument data (Fig. 6). Fig. 5 shows the standard deviation of albedo values of the high resolution datasets within individual pixels of the low albedo datasets. Figs. 5a and 5b show that the variability of albedo at 5 m resolution is broadly consistent with the different facies types identified. The transition zone has the highest albedo variability. The variability is slight less in the high albedo snow area. The zones of moderately dirty ice and dirty ice are much less variable, consistent with their lower overall albedo, although the contrasts near the

442 glacier margin result in a slightly greater variability there than in the moderately dirty ice area at
443 slightly higher elevations.

444 Fig. 5c shows that the albedo variability within the ETM6S dataset has fundamentally different
445 characteristics to that in the ATM6S dataset. In the ETM6S dataset, the moderately dirty and dirty
446 ice facies have low albedo variability. The high albedo snow facies has a highly variable albedo.
447 However, the degree of variability is subtly different from the ATM6S at 5 m resolutions. The albedo
448 of the snow facies is slightly less variable in the ETM6S dataset than in the ATM6S dataset. In
449 contrast, the dirty ice facies has a more variable albedo in the ETM6S dataset than in the ATM6S
450 dataset. The contrast between the two datasets is greatest for the transition zone; the ETM6S
451 dataset implies an increase in variability in the transition zone but the variability is much lower than
452 that shown by the ATM6S dataset. Thus it appears that the greater the variability in albedo is within
453 a large pixel, the greater (or smaller) the bias is in the low resolution dataset. The relationship
454 between variability and bias is dependent on which facies or zone on the ice cap which is being
455 measured and provides the basis for understanding Fig. 6.

456 Comparisons of the ATM6S, ETM6S and MCD43 datasets show consistent differences in measured
457 albedos across individual facies types. Different surface facies across the icecap have both different
458 albedos but also different anisotropic scattering regimes. Both snow and ice are forward scatterers,
459 however, the degree of forward scattering is controlled by numerous factors. The BRDF of snow and
460 ice is dependent on grain size, shape and orientation and the debris and water content (Knap and
461 Reijmer 1998; Warren and Wiscombe 1980; Wiscombe and Warren 1980). It will also vary according
462 to instrument view angle, and solar azimuth and zenith angles (Greuell et al. 2002). In order to
463 reliably correct remotely sensed data for variable anisotropic scattering, BRDF function for different
464 facies types appropriate to a range of possible variables, i.e. different debris contents, are needed. A
465 limited number of BRDF functions are available for clean dry snow (Marks et al. 2015), melting snow
466 surfaces (Dumont et al. 2012) and glacier ice with different surface water and debris contents

(Greuell and de Wildt 1999; Greuell et al. 2002). However, the practical application of these BRDF function is limited by our ability to correctly identify the specific characteristics of the surface in question(Greuell et al. 2002). The effect of variable BRDFs on remotely sensed snow and ice albedo therefore remains a source of large uncertainty especially in locations with highly variable surfaces such as Langjökull.

The effects of variable BRDF together with those of surface geometry and roughness combine to influence the direction and strength of reflection (Arnold et al. 2006; Lhermitte et al. 2014). Thus, for facies where both albedo and anisotropic scattering change over very small spatial scales, only a high resolution instruments will capture the changing reflective characteristics of the surface despite the BRDF correction implemented as part of the MCD43 processes. Each surface characteristic acts as a single influence on the albedo measured over a small area and it is the additive nature of these influences that controls the extent to which a single low resolution pixel will be able to capture the average albedo measured at a higher resolution across the area of the larger pixel. The differences between the datasets is therefore a consequence of a range of influences on reflection characteristics that change over small spatial scales which low resolution datasets are able unable to measure accurately.

4.2. Evaluation of MCD43 product

When averaged across the whole of Langjökull, albedos tended to be overestimated by the MCD43 product when compared to the ATM6S and ETM6S albedos (Table 4). This finding is in agreement with Stroeve et al.'s (2013) re-evaluation of the MCD43 product, which suggested that the MCD43 product overestimates albedo for snow and ice when compared to ground-based albedo measurements. However, while the Stroeve et al. (2013) study suggested the biases were due to the unique nature of the precise *in situ* measurement sites compared to the rest of each pixel area, we suggest that the differences seen are a consequence of albedo variability specific to individual surface facies types. This is a consequence of surface albedo changes at very small scales and the

associated changes in anisotropy as well as different surface types having different degrees of anisotropy. These characteristics mean that a single BRDF or a lower spatial resolution will be different from the various BRDF shapes that exist for the surface characteristics at finer scales. Assessment of the overall mean albedo value of glacier and ice cap surface by the MCD43 is therefore dependent on the proportion of the different facies type and the related anisotropic effects which cover the surface.

4.3. Implications for energy balance modelling and melt estimates

The differences shown between the ATM6S, ETM6S and MCD43 albedos across Langjökull have implications for energy balance modelling. Energy balance models contain large uncertainties. These uncertainties are due to the effects of spatially and temporally varying factors such as topographic shading, cloud cover, wind speed and, crucially, surface characteristics, notably albedo (Arnold et al. 2006; Hock and Holmgren 2005; Klok and Oerlemans 2002; Pellicciotti et al. 2005; 2008; Rye et al. 2010). The influence of each of these factors changes according to location, time and climate. For individual glaciers, high resolution energy balance models (typically at scales of a few tens of metres) often parameterise albedo variability using site specific meteorological data and surface information derived from *in situ* measurements (Hock and Holmgren 2005; MacDougall and Flowers 2011). However, little has been done to investigate the extent to which measured changes at specific points are representative of the surface change glacier wide, e.g. Hakala et al. (2014). At coarser resolutions (often $\geq 0.5^{o}$) regional climate models calculate albedo using simple physical principles (Aas et al. 2015; van Angelen et al. 2012). The coarse resolution of these models makes accurate incorporation of an albedo term challenging. Both high resolution and coarse resolution models are therefore likely to have biases in their treatment of albedo, similar to those shown by the different resolution measurements discussed in this study.

Our results indicate that even if we consider only the differences between the mean albedo values across Langjökull, the differences between the datasets could have a large impact on predicted melt

517 if they were used to validate/calibrate a surface energy balance model. Differences in net-shortwave
518 radiation induced melt were estimated by assuming Langjökull had a uniform horizontal surface with
519 no shading and an incoming shortwave flux of 140 Wm^{-2} for 31 days. 140 Wm^{-2} represents an
520 average figure for Langjökull in August (Rolstad and Oerlemans 2005). The results are shown in Table
521 8.

522 *Table 8. Differences in melt induced by net-shortwave radiation which would be generated by using*
523 *estimates of mean surface albedo derived from the ATM6S, ETM6S and MCD43 datasets assuming*
524 *an incoming shortwave flux of 140 Wm^{-2} for 31 days.*

Dataset Comparison	**Difference in melt (mm.w.e)**	**Difference in melt across the ice cap (m^3)**
ATM6S – ETM6S	0.528	4.884×10^6
ATM6S – MCD43	1.308	1.210×10^5
ETM6S – MCD43	0.781	7.224×10^5

525

526 The biases towards higher mean albedos in the coarser resolution datasets compared with a finer
527 resolution dataset would result in large under-predictions of melt over a single ablation season. The
528 different biases across the different faces would have additional impacts, with melt being predicted
529 in some locations and under predicted in others if coarse resolution albedo data are used to
530 validate/calibrate a surface energy balance model. Further efforts should be made to determine just
531 how important such albedo biases are for surface energy balance modelling.

532 **5. Conclusions**

533 This study has explored the ability of different resolution instruments and different retrieval
534 methods to measure the surface albedo across Langjökull. Different retrieval methods for the same
535 instrument have been shown to produce inconsistent surface albedo measurements. These
536 differences are the result of contrasts between different atmospheric correction models which were
537 applied. Correction of both ATM and ETM+ datasets using FLAASH produced mean albedos greater
538 than those generated by 6S. Comparison of a 6S corrected ATM dataset, a 6S corrected ETM+
539 dataset and an MCD43 dataset showed contrasting albedo values between the datasets associated

with specific glacier facies. These differences are suggested to be the result of the degree to which sub-pixel scale differences in albedo, BRDFs, surface geometry and surface roughness can be captured by the different measurement platforms with different spatial resolutions.

The albedo of snow and ice changes substantially during the melt season. Few studies have been able to model albedo changes over very small spatial scales, particularly for different ice facies. Comparison of the datasets in this study demonstrates the importance of recognising the heterogeneity of surface albedo. Understanding the effects of albedo variability over small spatial scales is therefore crucial to understanding albedo evolution and feedbacks at larger spatial scales and their overall effects on glacier mass balance. It is important for future studies, where possible, to assess surface reflectance characteristics derived from different resolution instruments in order to assess whether the any systematic biases we have identified on Langjökull are present elsewhere. This will be crucial to future monitoring and modelling of albedo, energy balance and mass balance of the world's glaciers.

Acknowledgements

This work was supported by the UK NERC ARSF – Project IPY07-08. E. Pope was supported by the NERC Arctic Research Programme under project NE/K00008X/1. A. Pope was supported by the National Science Foundation Graduate Research Fellowship Programme under Grant No. DGE-1038596 and by Trinity College, Cambridge. E. Miles was supported by a Gates Cambridge Scholarship and by Trinity College, Cambridge. Fieldwork associated with the ATM flights was supported by grants from the University of Cambridge Scandinavian Studies Fund and the B. B. Roberts Fund. Finally, we would also like to thank NASA LP DAAC for the freely available MODIS and Landsat data used. We thank the editor Dorothy Hall and two anonymous reviewers whose comments greatly helped improve the manuscript.

References

Aas, K.S., Berntsen, T.K., Boike, J., Etzelmüller, B., Kristjánsson, J.E., Maturilli, M., Schuler, T.V., Stordal, F., & Westermann, S. (2015). A comparison between simulated and observed surface energy balance at the Svalbard archipelago. *Journal of Applied Meteorology and Climatology*

Aniya, M., Sato, H., Naruse, R., Skvarca, P., & Casassa, G. (1996). The use of satellite and airborne imagery to inventory outlet glaciers of the Southern Patagonia Icefield, South America. *Photogrammetric Engineering and Remote Sensing, 62*, 1361-1369

Arendt, A. (1999). Approaches to modelling the surface albedo of a high Arctic glacier. *Geografiska Annaler Series a-Physical Geography, 81A*, 477-487

Arnold, N.S., & Rees, W.G. (2003). Self-similarity in glacier surface characteristics. *Journal of Glaciology, 49*, 547-554

Arnold, N.S., Rees, W.G., Hodson, A.J., & Kohler, J. (2006). Topographic controls on the surface energy balance of a high Arctic valley glacier. *Journal of Geophysical Research-Earth Surface, 111*

Björnsson, H., & Pálsson, F. (2008). Icelandic glaciers. *Jokull, 58*, 365-386

Box, J.E., Fettweis, X., Stroeve, J.C., Tedesco, M., Hall, D.K., & Steffen, K. (2012). Greenland ice sheet albedo feedback: thermodynamics and atmospheric drivers. *Cryosphere, 6*, 821-839

Boyd, D.S. (2009). Remote sensing in physical geography: a twenty-first-century perspective. *Progress in Physical Geography, 33*, 451-456

Brock, B.W., Willis, I.C., Sharp, M.J., & Arnold, N.S. (2000). Modelling seasonal and spatial variations in the surface energy balance of Haut Glacier d'Arolla, Switzerland. *Annals of Glaciology, Vol 31, 2000, 31*, 53-62

Chander, G., Markham, B.L., & Helder, D.L. (2009). Summary of current radiometric calibration coefficients for Landsat MSS, TM, ETM+, and EO-1 ALI sensors. *Remote Sensing of Environment, 113*, 893-903

Cuffey, K.M., & Paterson, W.S.B. (2010). *The physics of glaciers*. Academic Press

Cutler, P.M., & Munro, D.S. (1996). Visible and near-infrared reflectivity during the ablation period on Peyto Glacier, Alberta, Canada. *Journal of Glaciology, 42*, 333-340

Dowdeswell, J.A., Hagen, J.O., Björnsson, H., Glazovsky, A.F., Harrison, W.D., Holmlund, P., Jania, J., Koerner, R.M., Lefauconnier, B., & Ommanney, C.S.L. (1997). The mass balance of circum-Arctic glaciers and recent climate change. *Quaternary Research, 48*, 1-14

Dumont, M., Durand, Y., Arnaud, Y., & Six, D. (2012). Variational assimilation of albedo in a snowpack model and reconstruction of the spatial mass-balance distribution of an alpine glacier. *Journal of Glaciology, 58*, 151-164

Flowers, G.E., Bjornsson, H., Geirsdottir, A., Miller, G.H., & Clarke, G.K.C. (2007). Glacier fluctuation and inferred climatology of Langjokull ice cap through the Little Ice Age. *Quaternary Science Reviews, 26*, 2337-2353

Graversen, R.G., Mauritsen, T., Tjernström, M., Källén, E., & Svensson, G. (2008). Vertical structure of recent Arctic warming. *Nature, 451*, 53-56

Greuell, W., & de Wildt, M.d.R. (1999). Anisotropic reflection by melting glacier ice: Measurements and parametrizations in Landsat TM bands 2 and 4. *Remote Sensing of Environment, 70*, 265-277

Greuell, W., & Oerlemans, J. (2004). Narrowband-to-broadband albedo conversion for glacier ice and snow: equations based on modeling and ranges of validity of the equations. *Remote Sensing of Environment, 89*, 95-105

Greuell, W., Reijmer, C.H., & Oerlemans, J. (2002). Narrowband-to-broadband albedo conversion for glacier ice and snow based on aircraft and near-surface measurements. *Remote Sensing of Environment, 82*, 48-63

Guðmundsson, S., Björnsson, H., Pálsson, F., and Haraldsson, H.H. (2009). Comparison of energy balance and degree-day model of summer ablation on the Langjökull ice cap, SW-Iceland. *Jokull, 59*, 1-18

Hagen, J.O., Melvold, K., Pinglot, F., & Dowdeswell, J.A. (2003). On the net mass balance of the glaciers and ice caps in Svalbard, Norwegian Arctic. *Arctic, Antarctic, and Alpine Research, 35*, 264-270

Hakala, T., Riihelä, A., Lahtinen, P., & Peltoniemi, J.I. (2014). Hemispherical-directional reflectance factor measurements of snow on the Greenland Ice Sheet during the Radiation, Snow Characteristics and Albedo at Summit (RASCALS) campaign. *Journal of Quantitative Spectroscopy and Radiative Transfer, 146*, 280-289

Hall, D.K., Chang, A.T.C., Foster, J.L., Benson, C.S., & Kovalick, W.M. (1989). Comparison of In situ and Landsat Derived Reflectance of Alaskan Glaciers. *Remote Sensing of Environment, 28*, 23-31

Hendriks, J., & Pellikka, P. (2004). Estimation of reflectance from a glacier surface by comparing spectrometer measurements with satellite-derived reflectances. *Journal of Glaciology, 38*, 139-154

Hill, R.A., Wilson, A.K., George, M., & Hinsley, S.A. (2010). Mapping tree species in temperate deciduous woodland using time-series multi-spectral data. *Applied Vegetation Science, 13*, 86-99

Hock, R., & Holmgren, B. (2005). A distributed surface energy-balance model for complex topography and its application to Storglaciären, Sweden. *Journal of Glaciology, 51*, 25-36

Kennedy, R.E., Cohen, W.B., & Takao, G. (1997). Empirical methods to compensate for a view-angle-dependent brightness gradient in AVIRIS imagery. *Remote Sensing of Environment, 62*, 277-291

Klok, E.J., & Oerlemans, J. (2002). Model study of the spatial distribution of the energy and mass balance of Morteratschgletscher, Switzerland. *Journal of Glaciology, 48*, 505-518

Knap, W.H., Brock, B.W., Oerlemans, J., & Willis, I.C. (1999). Comparison of Landsat TM-derived and ground-based albedos of Haut Glacier d'Arolla, Switzerland. *International Journal of Remote Sensing, 20*, 3293-3310

Knap, W.H., & Reijmer, C.H. (1998). Anisotropy of the reflected radiation field over melting glacier ice: Measurements in Landsat TM bands 2 and 4. *Remote Sensing of Environment, 65*, 93-104

Kotchenova, S.Y., & Vermote, E.F. (2007). Validation of a vector version of the 6S radiative transfer code for atmospheric correction of satellite data. Part II. Homogeneous Lambertian and anisotropic surfaces. *Applied Optics, 46*, 4455-4464

Lee, D.S., Storey, J.C., Choate, M.J., & Hayes, R.W. (2004). Four years of Landsat-7 on-orbit geometric calibration and performance. *Ieee Transactions on Geoscience and Remote Sensing, 42*, 2786-2795

Lhermitte, S., Abermann, J., & Kinnard, C. (2014). Albedo over rough snow and ice surfaces. *The Cryosphere, 8*, 1069-1086

Liang, S.L., Stroeve, J., & Box, J.E. (2005). Mapping daily snow/ice shortwave broadband albedo from Moderate Resolution Imaging Spectroradiometer (MODIS): The improved direct retrieval algorithm and validation with Greenland in situ measurement. *Journal of Geophysical Research-Atmospheres, 110*

Lucht, W., Schaaf, C.B., & Strahler, A.H. (2000). An algorithm for the retrieval of albedo from space using semiempirical BRDF models. *Ieee Transactions on Geoscience and Remote Sensing, 38*, 977-998

MacDougall, A.H., & Flowers, G.E. (2011). Spatial and Temporal Transferability of a Distributed Energy-Balance Glacier Melt Model. *Journal of Climate, 24*, 1480-1498

Mahiny, A.S., & Turner, B.J. (2007). A comparison of four common atmospheric correction methods. *Photogrammetric Engineering and Remote Sensing, 73*, 361-368

Marks, A., Fragiacomo, C., MacArthur, A., Zibordi, G., Fox, N., & King, M.D. (2015). Characterisation of the HDRF (as a proxy for BRDF) of snow surfaces at Dome C, Antarctica, for the inter-calibration and inter-comparison of satellite optical data. *Remote Sensing of Environment, 158*, 407-416

Matthew, M.W., Adler-Golden, S.M., Berk, A., Richtsmeier, S.C., Levine, R.Y., Bernstein, L.S., Acharya, P.K., Anderson, G.P., Felde, G.W., Hoke, M.P., Ratkowski, A., Burke, H.H., Kaiser, R.D., & Miller, D.P. (2000). Status of atmospheric correction using a MODTRAN4-based algorithm. *Algorithms for Multispectral, Hyperspectral, and Ultraspectral Imagery Vi, 4049*, 199-207

Meier, M.F., Dyurgerov, M.B., Rick, U.K., O'Neel, S., Pfeffer, W.T., Anderson, R.S., Anderson, S.P., & Glazovsky, A.F. (2007). Glaciers dominate eustatic sea-level rise in the 21st century. *Science, 317*, 1064-1067

Palubinskas, G., Muller, R., & Reinartz, P. (2003a). Mosaicking of optical remote sensing imagery. *Igarss 2003: Ieee International Geoscience and Remote Sensing Symposium, Vols I - Vii, Proceedings*, 3955-3957

Palubinskas, G., Muller, R., & Reinartz, P. (2003b). Radiometric normalization of optical remote sensing imagery. *Igarss 2003: Ieee International Geoscience and Remote Sensing Symposium, Vols I - Vii, Proceedings*, 720-722

Paul, F., Kaab, A., Maisch, M., Kellenberger, T., & Haeberli, W. (2004). Rapid disintegration of Alpine glaciers observed with satellite data. *Geophysical Research Letters, 31*

Pellicciotti, F., Brock, B.W., Strasser, U., Burlando, P., Funk, M., & Corripio, J. (2005). An enhanced temperature-index glacier melt model including the shortwave radiation balance: Development and testing for Haut Glacier d'Arolla, Switzerland. *Journal of Glaciology, 51*, 573-587

Pellicciotti, F., Helbing, J., Rivera, A., Favier, V., Corripio, J., Araos, J., Sicart, J.E., & Carenzo, M. (2008). A study of the energy balance and melt regime on Juncal Norte Glacier, semi-arid Andes of central Chile, using melt models of different complexity. *Hydrological processes, 22*, 3980-3997

Perkins, T., Adler-Golden, S.M., Cappelaere, P., & Mandl, D. (2012). High-speed atmospheric correction for spectral image processing. In, *Proc. of SPIE Vol* (pp. 83900V-83901)

Pope, A., Willis, I.C., Rees, W.G., Arnold, N.S., & Palsson, F. (2013). Combining airborne lidar and Landsat ETM plus data with photoclinometry to produce a digital elevation model for Langjokull, Iceland. *International Journal of Remote Sensing, 34*, 1005-1025

Privette, J.L., Eck, T.F., & Deering, D.W. (1997). Estimating spectral albedo and nadir reflectance through inversion of simple BRDF models with AVHRR/MODIS-like data. *Journal of Geophysical Research-Atmospheres, 102*, 29529-29542

Radić, V., & Hock, R. (2011). Regionally differentiated contribution of mountain glaciers and ice caps to future sea-level rise. *Nature Geoscience, 4*, 91-94

Rees, W.G.S. (2006). *Remote sensing of snow and ice*. Boca Raton: Taylor & Francis

Reijmer, C.H., Knap, W.H., & Oerlemans, J. (1999). The surface albedo of the Vatnajokull ice cap, Iceland: A comparison between satellite-derived and ground-based measurements. *Boundary-Layer Meteorology, 92*, 125-144

Rolstad, C., & Oerlemans, J. (2005). The residual method for determination of the turbulent exchange coefficient applied to automatic weather station data from Iceland, Switzerland and West Greenland. *Annals of Glaciology, 42*, 367-372

Roujean, J.L., Leroy, M., & Deschamps, P.Y. (1992). A bidirectional reflectance model of the Earth's surface for the correction of remote sensing data. *Journal of Geophysical Research: Atmospheres (1984–2012), 97*, 20455-20468

Rye, C.J., Arnold, N.S., Willis, I.C., & Kohler, J. (2010). Modeling the surface mass balance of a high Arctic glacier using the ERA-40 reanalysis. *Journal of Geophysical Research: Earth Surface (2003–2012), 115*

Salomon, J.G., Schaaf, C.B., Strahler, A.H., Gao, F., & Jin, Y.F. (2006). Validation of the MODIS bidirectional reflectance distribution function and albedo retrievals using combined observations from the Aqua and Terra platforms. *Geoscience and Remote Sensing, IEEE Transactions on, 44*, 1555-1565

Schaaf, C.B., Gao, F., Strahler, A.H., Lucht, W., Li, X.W., Tsang, T., Strugnell, N.C., Zhang, X., Jin, Y.F., & Muller, J.-P. (2002). First operational BRDF, albedo nadir reflectance products from MODIS. *Remote Sensing of Environment, 83*, 135-148

Schaepman-Strub, G., Schaepman, M., Painter, T., Dangel, S., & Martonchik, J. (2006). Reflectance quantities in optical remote sensing—Definitions and case studies. *Remote Sensing of Environment, 103*, 27-42

Serreze, M.C., Holland, M.M., & Stroeve, J. (2007). Perspectives on the Arctic's shrinking sea-ice cover. *Science, 315*, 1533-1536

Shimamura, Y., Izumi, T., & Matsuyama, H. (2006). Evaluation of a useful method to identify snow-covered areas under vegetation–comparisons among a newly proposed snow index, normalized

716 difference snow index, and visible reflectance. *International Journal of Remote Sensing, 27*, 4867-
717 4884
718 Strahler, A.H., Muller, J.P., Lucht, W., Schaaf, C.B., Tsang, T., Gao, F., Li, X.W., Lewis, P., & Barnsley,
719 M.J. (1999). MODIS BRDF/albedo product: algorithm theoretical basis document version 5.0. *MODIS*
720 *documentation*
721 Stroeve, J., Box, J.E., Gao, F., Liang, S.L., Nolin, A., & Schaaf, C. (2005). Accuracy assessment of the
722 MODIS 16-day albedo product for snow: comparisons with Greenland in situ measurements. *Remote*
723 *Sensing of Environment, 94*, 46-60
724 Stroeve, J., Box, J.E., Wang, Z., Schaaf, C., & Barrett, A. (2013). Re-evaluation of MODIS MCD43
725 Greenland albedo accuracy and trends. *Remote Sensing of Environment, 138*, 199-214
726 Tedesco, M., Fettweis, X., van den Broeke, M.R., van de Wal, R.S.W., Smeets, C.J.P.P., van de Berg,
727 W.J., Serreze, M.C., & Box, J.E. (2011). The role of albedo and accumulation in the 2010 melting
728 record in Greenland. *Environmental Research Letters, 6*
729 Tucker, C.J., Grant, D.M., & Dykstra, J.D. (2004). NASA's global orthorectified Landsat data set.
730 *Photogrammetric Engineering and Remote Sensing, 70*, 313-322
731 van Angelen, J.H., Lenaerts, J.T.M., Lhermitte, S., Fettweis, X., Munneke, P.K., van den Broeke, M.R.,
732 van Meijgaard, E., & Smeets, C.J.P.P. (2012). Sensitivity of Greenland Ice Sheet surface mass balance
733 to surface albedo parameterization: a study with a regional climate model. *Cryosphere, 6*, 1175-1186
734 Vermote, E., Tanré, D., Deuzé, J., Herman, M., Morcrette, J., & Kotchenova, S. (2006). Second
735 simulation of a satellite signal in the solar spectrum-vector (6SV). *6S User Guide Version, 3*
736 Vermote, E.F., El Saleous, N.Z., & Justice, C.O. (2002). Atmospheric correction of MODIS data in the
737 visible to middle infrared: first results. *Remote Sensing of Environment, 83*, 97-111
738 Warren, S.G., & Wiscombe, W.J. (1980). A model for the spectral albedo of snow. II: Snow containing
739 atmospheric aerosols. *Journal of the Atmospheric Sciences, 37*, 2734-2745
740 Wiscombe, W.J., & Warren, S.G. (1980). A model for the spectral albedo of snow. I: Pure snow.
741 *Journal of the Atmospheric Sciences, 37*, 2712-2733
742 Wolken, G.J., Sharp, M.J., & Wang, L. (2009). Snow and ice facies variability and ice layer formation
743 on Canadian Arctic ice caps, 1999–2005. *Journal of Geophysical Research: Earth Surface, 114*, F03011
744 Zelazowski, P., Sayer, A.M., Thomas, G.E., & Grainger, R.G. (2011). Reconciling satellite-derived
745 atmospheric properties with fine-resolution land imagery: Insights for atmospheric correction.
746 *Journal of Geophysical Research-Atmospheres, 116*
747 Zhao, Y., Meng, Z., Wang, L., Miyazaki, S., Geng, X., Zhou, G., Liu, R., Kosaka, N., Takahashi, M., & Li,
748 X. (2005). A new cross-track radiometric correction method (VRadCor) for airborne hyperspectral
749 image of operational modular imaging spectrometer (OMIS). *Proceedings of IEEE IGARSS*, 3553-3356

750

751

752 **Figure Captions**

753 Fig 1. Langjökull a) Geographic setting, Landsat ETM+ real colour image from 20 August 2000 (path
754 220, row 15); b) delineated drainage basins.

755 Fig 2. Surface albedo maps of Langjökull. a) ATM surface albedo map derived using FLAASH; b) ATM
756 surface albedo map derived using 6S; c) ETM+ surface albedo map derived using FLAASH; d) ETM+
757 surface albedo map derived using 6S; e) MCD43 MODIS albedo map. Black areas represent the full
758 extent of Langjökull but which no data exists in one or all of the datasets due to cloud cover and SLC-
759 error on the ETM+ image.

760 Fig 3. Histograms of pixel albedo values. a) ATMFlaash; b) ATM6S; c) ETMFlaash; d) ETM6S; e)
761 MCD43.

762 Fig 4. Surface albedo across the area of a single MCD43 pixel in the ablation area of Eystri-
763 Hagafellsjökull. a) ATM6S representation of surface albedo; b) ETM6S representation of surface
764 albedo; c) surface albedo for the MCD43 pixel. The location of the MCD43 pixel is shown in Fig 2e.

765 Fig. 5. Map of the standard deviation of pixel values of the high resolution datasets within individual
766 low resolution pixels. a) ATM6S pixel standard deviation within 30 m ETM6S pixels; b) ATM6S pixel
767 standard deviation within 500 m MCD43 pixels; c) ETM6S standard deviation within 500 m MCD43
768 pixels.

769 Fig. 6. Map of differences in albedo values between different datasets. a) ATM6S and ETM6S; b)
770 ATM6S and MCD43; c) ETM6S and MCD43.

771

772

773

774 Figures

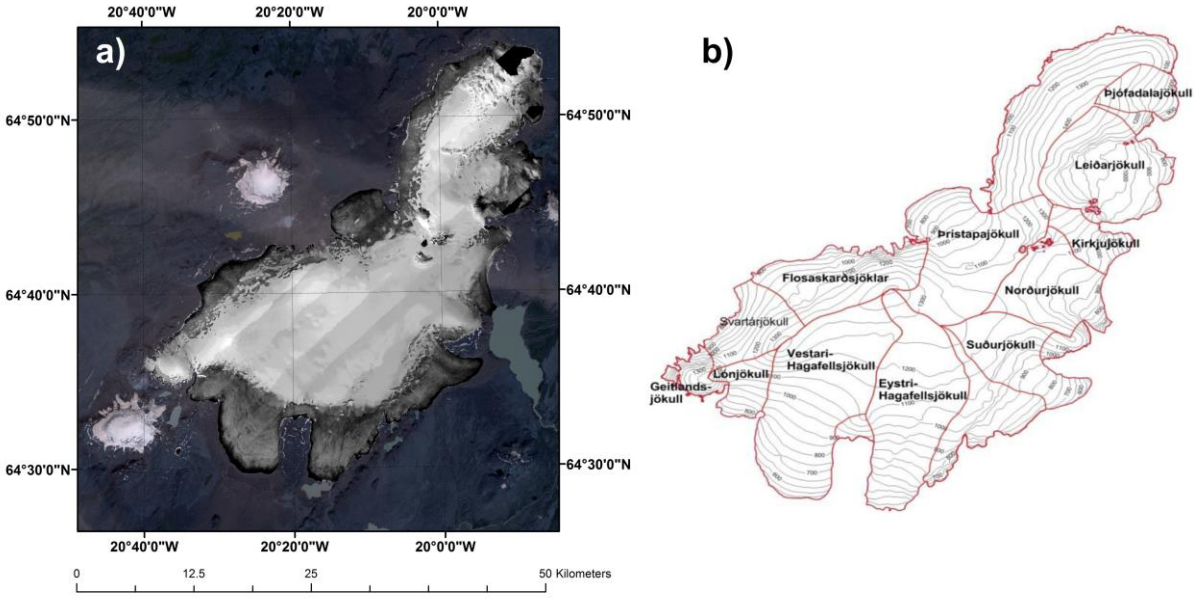

775

776 Fig 1. Langjökull a) Geographic setting, Landsat ETM+ real colour image from 20 August 2000 (path

777 220, row 15); b) delineated drainage basins.

778

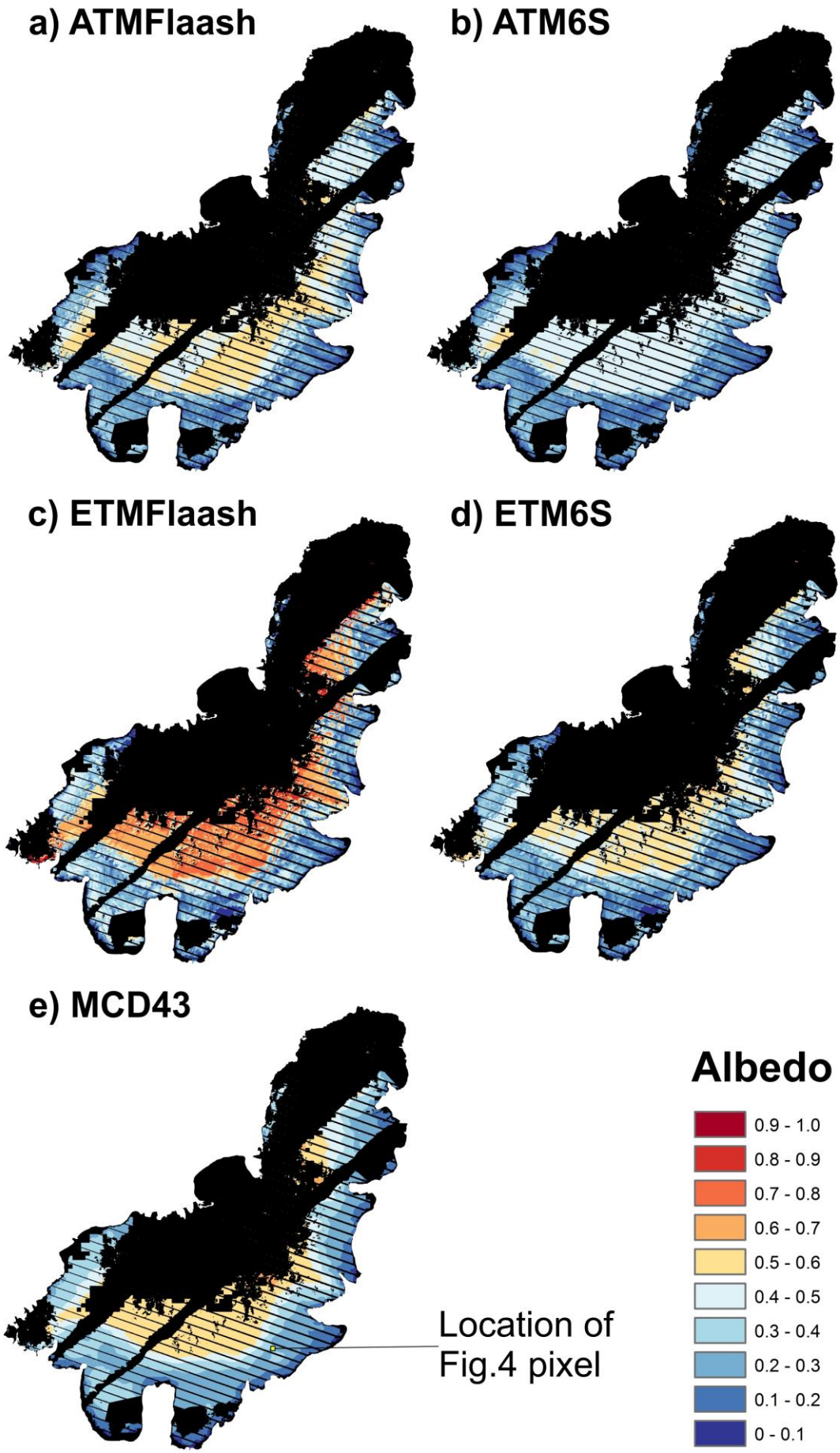
a) ATMFlaash
b) ATM6S
c) ETMFlaash
d) ETM6S
e) MCD43
Location of
Fig.4 pixel
Albedo
0.9 - 1.0
0.8 - 0.9
0.7 - 0.8
0.6 - 0.7
0.5 - 0.6
0.4 - 0.5
0.3 - 0.4
0.2 - 0.3
0.1 - 0.2
0 - 0.1

779

780 Fig 2. Surface albedo maps of Langjökull. a) ATM surface albedo map derived using FLAASH; b) ATM
781 surface albedo map derived using 6S; c) ETM+ surface albedo map derived using FLAASH; d) ETM+
782 surface albedo map derived using 6S; e) MCD43 MODIS albedo map. Black areas represent the full
783 extent of Langjökull but which no data exists in one or all of the datasets due to cloud cover and SLC-
784 error on the ETM+ image.

785

786

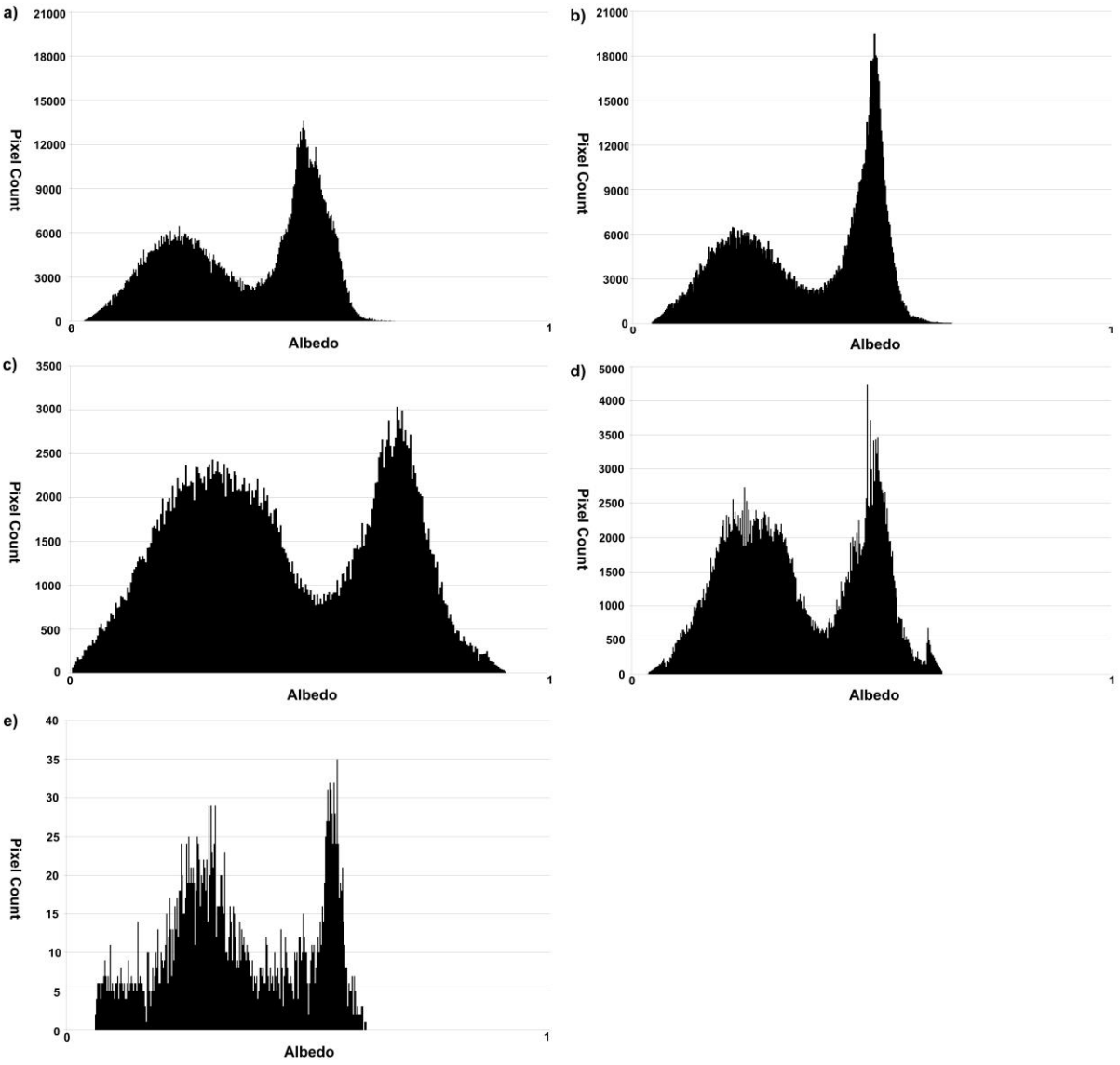

787

788 Fig 3. Histograms of pixel albedo values. a) ATMFlaash; b) ATM6S; c) ETMFlaash; d) ETM6S; e)
789 MCD43.

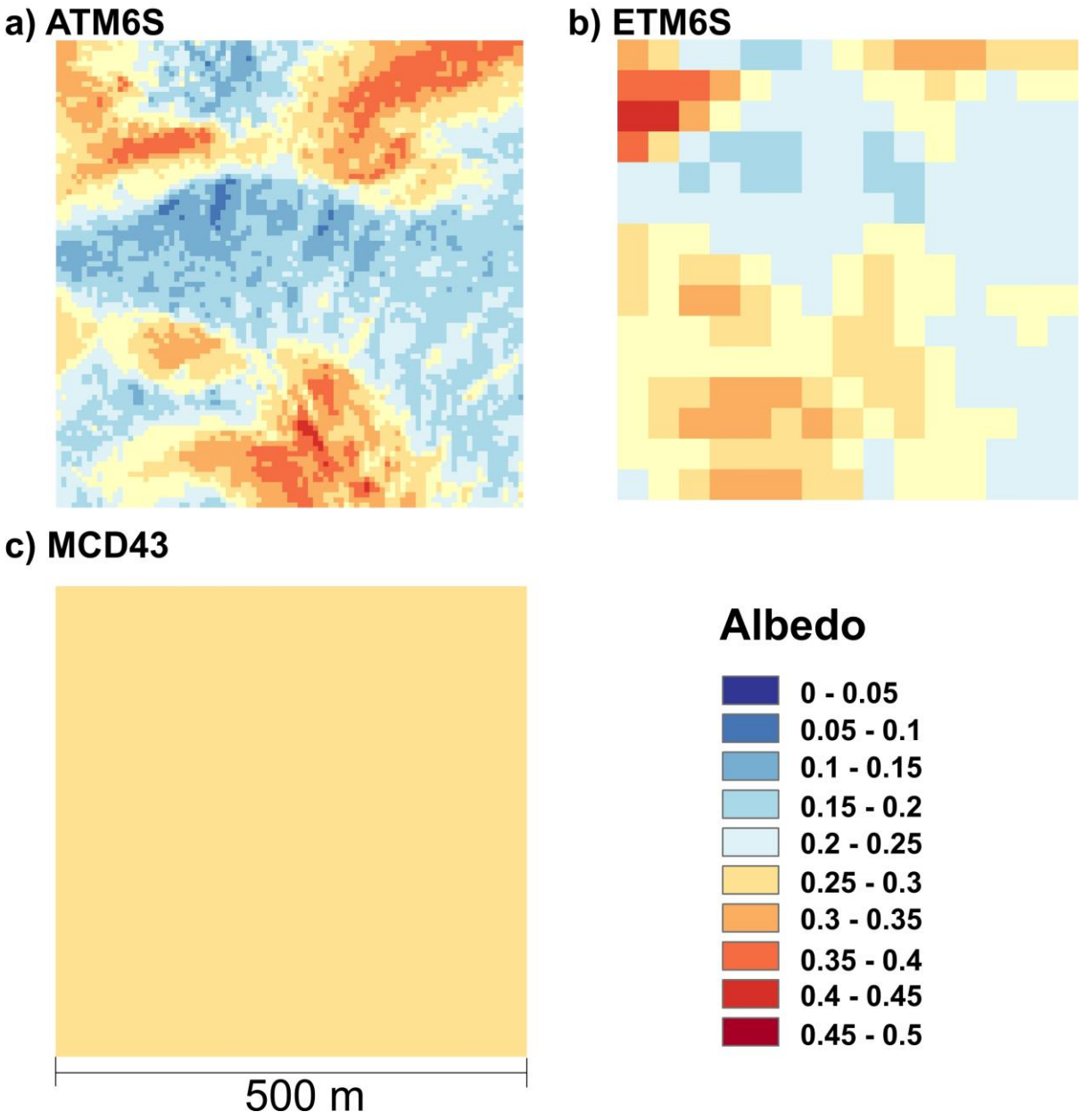

790

791

792 Fig 4. Surface albedo across the area of a single MCD43 pixel in the ablation area of Eystri-

793 Hagafellsjökull. a) ATM6S representation of surface albedo; b) ETM6S representation of surface

794 albedo; c) surface albedo for the MCD43 pixel. The location of the MCD43 pixel is shown in Fig 2e.

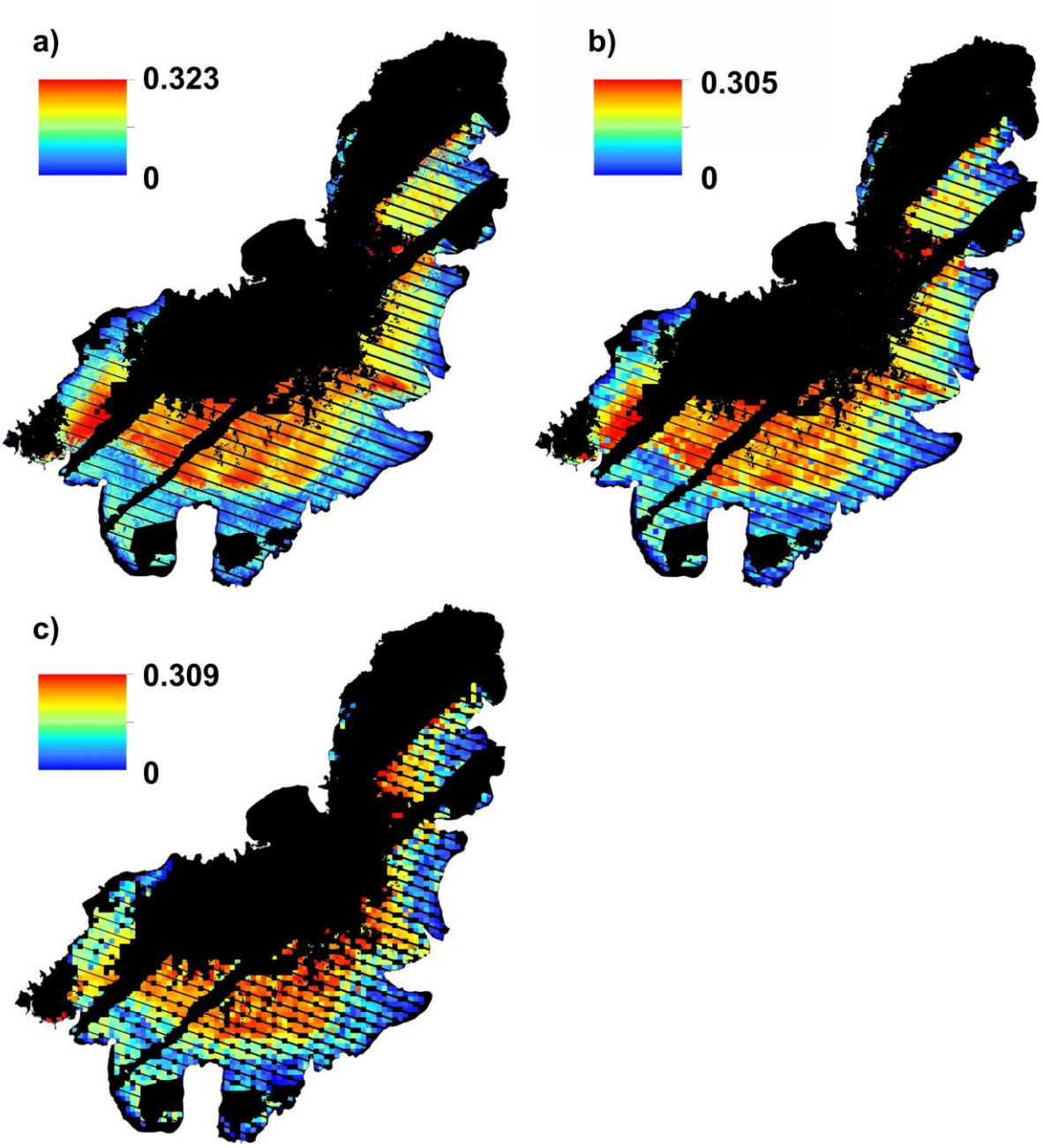

795

796

797 Fig. 5. Map of the standard deviation of pixel values of the high resolution datasets within individual

798 low resolution pixels. a) ATM6S pixel standard deviation within 30 m ETM6S pixels; b) ATM6S pixel

799 standard deviation within 500 m MCD43 pixels; c) ETM6S standard deviation within 500 m MCD43

800 pixels.

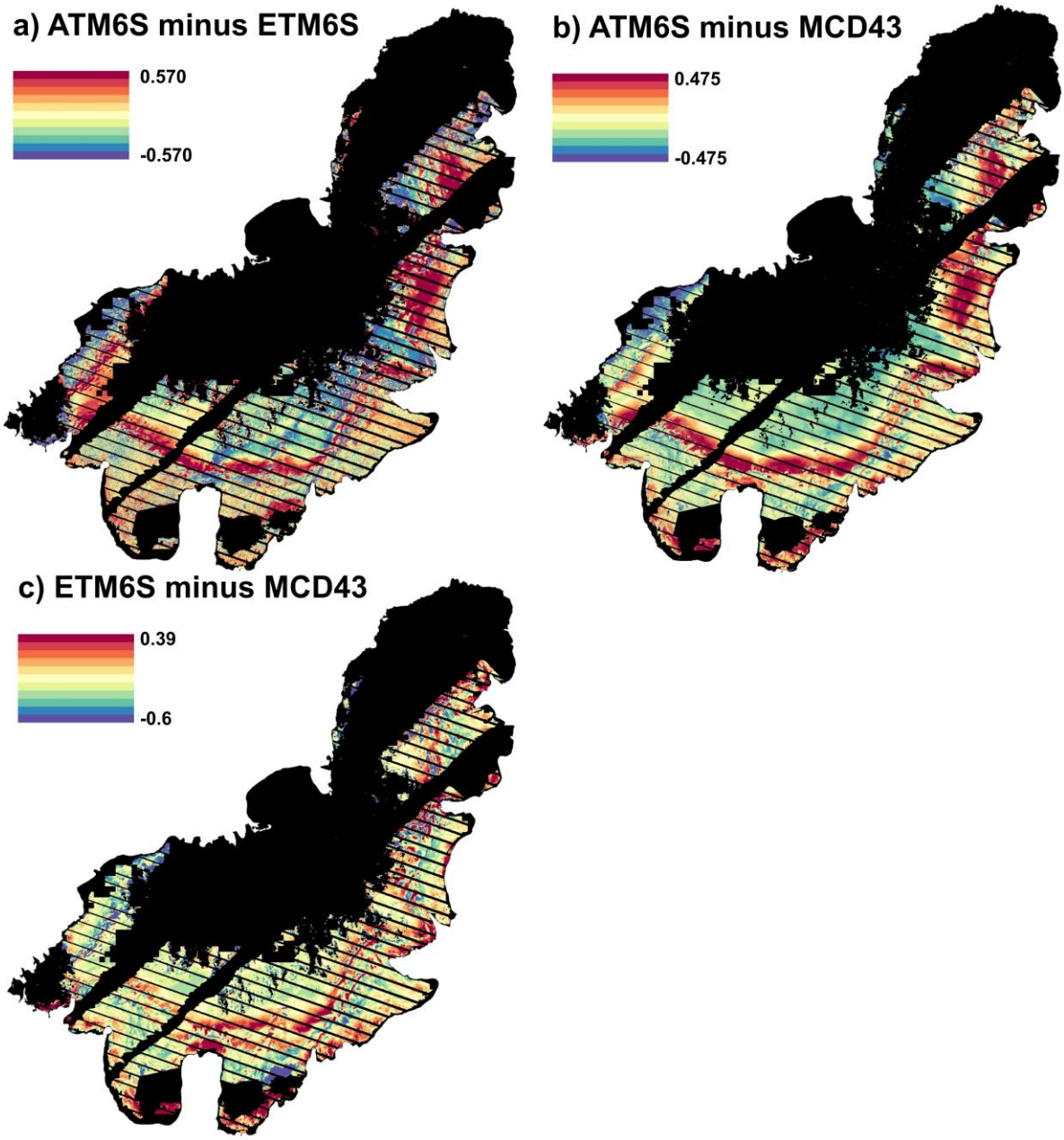

801

802

803 Fig. 6. Map of differences in albedo values between different datasets. a) ATM6S and ETM6S; b)

804 ATM6S and MCD43; c) ETM6S and MCD43.

805